*Research Article*

# The Influence of Ventilation Arrangement on the Mechanism of Dust Distribution in Woxi Pithead

**Zhiyong Zhou** [ID],[1] **Pei Hu,**[1] **Chongchong Qi** [ID],[2] **Tianpei Niu** [ID],[3] **Ming Li** [ID],[1] **and Long Tian**[1]

[1]*School of Resources and Safety Engineering, Central South University, Changsha 410083, China*
[2]*School of Civil, Environmental and Mining Engineering, The University of Western Australia, Perth 6009, Australia*
[3]*Xi'an Highway Bureau of Shaanxi Province, Xi'an 710003, China*

Correspondence should be addressed to Chongchong Qi; 21948042@student.uwa.edu.au and Tianpei Niu; xasglkcsjy@126.com

Suppressing and removing mine dust from the working face is an important task for underground mines worldwide. In this paper, a numerical study was carried out to investigate the influence of ventilation arrangement on the mechanism of dust distribution. The Woxi Pithead of Hunan Chenzhou Mining Co., Ltd, China, was used as a case study, which adopted a widely used far-pressing-near-absorption (FPNA) ventilation system. Based on the theory of gas-solid two-phase flow, the program ANSYS Fluent was utilized, and the three-dimensional airflow migration and dust diffusion numerical models were simulated. The established computational fluid dynamics (CFD) models were validated using the airflow velocity data and the dust concentration data monitored at different positions from the operating coal mine. A comprehensive sensitivity study was conducted to investigate the influence of four parameters on dust suppression, including the distance of pressure air duct outlet from working face ($L_{\text{p-outlet}}$), the distance of exhaust air duct inlet from working face ($L_{\text{e-inlet}}$), the ratio of pressing air volume to lab sorption air volume ($K$), and the installation height of the air duct ($H$). The optimum ventilation layout parameters were obtained through the simulation of the wind field and dust behaviour. The results show that there were four regions during the airflow field, namely, the jet zone, the recirculation zone, the vortex zone, and the mixing zone of pressure and exhaust airflow. All four parameters were found to have an important influence on the mass concentration of dust, and the optimum ventilation layout parameters were determined to be $L_{\text{p-outlet}} = 18$ m, $L_{\text{e-inlet}} = 3$ m, $K = 1.2$, and $H = 1.6$ m.

## 1. Introduction

With the increasing of underground mining depth and the development of fully mechanized excavation technology, the dust pollution becomes increasingly serious [1]. It is estimated that the mass concentration of dust during the blasting operation can be up to $2 \times 10^{-3}$ kg/m$^3$, which is far higher than the safety regulation values [2, 3]. In addition, ore drilling, secondary crushing, loading and unloading, and transportation will also generate a lot of dust. These harmful fine dust particles are widely distributed and difficult to discharge from the confined space, thus endangering the health of underground practitioners and posing serious risks to mining equipment [4, 5]. As a massive amount of dust can lead to serious explosion accidents, high-concentration mine dust is the primary threat to production safety. Furthermore,

production efficiency is affected by these mine dust due to the production delay caused by the above-mentioned worker injuries, equipment malfunctions and disastrous accidents [6].

A variety of methods have been proposed to suppress mine dust, which includes water spray, foam dust control system, and ventilation dusting system [7, 8]. Among the above mine dust suppression methods, the ventilation dusting system (VDS) is the most widely used method to remove underground dust. In practice, the VDS is playing a vital role in diluting and removing mine dust for many underground mines, ensuring a safe, stable, and high-efficient mine production [9, 10]. Though great advances in VDS have been achieved in the literature, the ventilation condition and the airflow field were not well investigated, which is fundamental for efficient VDS design [11]. Many

researchers have focused on the interaction between the airflow migration and dust removal effect. For instance, Toraño et al. [12] investigated the mechanism of airflow migration and dust behaviour through combing the experimental results and simulation results. Candra et al. [13] investigated the dust dispersion and produced an effective management system in the underground working face. Yu et al. [14] established an airflow-dust coupled simulation method to investigate the dust diffusion mechanism in fully mechanized excavation mining face. However, a comprehensive sensitivity study about the influence of ventilation parameters on the dust distribution is still lacking. Also, the optimization of ventilation parameters for a more efficient VDS design has not been investigated throughout. There is, consequently, a pressing need to investigate the influence of ventilation parameters on dust distribution and optimize ventilation parameters during VDS design for a better dust suppression.

In the present study, the Woxi Pithead of Hunan Chenzhou Mining Co., Ltd was taken as a case study, which has a long mining history and a large mining depth (oblique depth greater than 3000 m and vertical depth greater than 1000 m). The problem of ventilation is especially prominent for the Woxi Pithead due to the spatial complexity of the roadway layers. To control mine dust, a variety of methods have been adopted in Woxi Pithead, such as using hybrid local ventilation, increasing the air supply in the underground roadway, and extending the ventilation time. Although these measures have achieved some improvements in dust control, the ventilation cost is significantly increased with the application of the above methods. Furthermore, the dust removal efficiency is not satisfactory due to the lack of theoretical research on the law of ventilation and dust migration in the underground tunnel.

In this paper, the program ANSYS Fluent was used to investigate the influence of various ventilation parameters on airflow migration and dust control. Based on the theory of gas-solid two-phase flow and the Euler–Lagrange method, the discrete phase model was used to calculate the motion of dust particles. The dust behaviour of the hybrid ventilation was investigated under different ventilation arrangement parameters, which were then optimized for a better VDS design. This research can provide theoretical guidance for deep mining ventilation in the Woxi Pithead and can be as easily applied to underground mines with similar mining conditions.

This paper is arranged as follows. Section 2 introduces the basic theory of computational fluid dynamics (CFD) used for numerical simulation. Section 3 presents the numerical models and simulation scenarios. The validation and verification of the numerical modelling are shown in Section 4, followed by Section 5 that presents the results and discussion. Section 6 concludes the main findings of this paper.

## 2. Computational Theory

The numerical model of the dust removal is based on the typical gas-solid two-phase flow. With a dust volume fraction of 10%, the discrete phase model was applied to calculate the dust behaviour [15, 16]. The airflow, as a primary phase, was simulated along with the standard k-epsilon model. To predict and track the trajectory of dust, the discrete model was used. The coupling of k-epsilon mode and the discrete model was carried out by solving the continuous phase equations first until convergence and the discrete model was then set to track the dust behaviour.

*2.1. The Model of Airflow Field.* The numerical model of airflow in this study is based on three governing laws, including the mass conservation equation, the momentum equation, and the energy equation, which can be defined as follows [17]:

$$\frac{\partial \rho}{\partial t} + \nabla \cdot (\rho \overrightarrow{v}) = 0,$$

$$\frac{\partial}{\partial t}(\rho \overrightarrow{v}) + \nabla \cdot (\rho \overrightarrow{v}\overrightarrow{v}) = -\nabla p + \nabla \cdot \mu \left[ \left( \nabla \overrightarrow{v} + \nabla \overrightarrow{v}^{\mathrm{T}} \right) - \frac{2}{3} \cdot \nabla \overrightarrow{v} \cdot I \right] + \rho \overrightarrow{g} + \overrightarrow{F},$$

$$\frac{\partial}{\partial t}(\rho T) + \nabla \cdot (\rho \overrightarrow{v} T) = \nabla \left( \frac{k_{\mathrm{T}}}{c_{\mathrm{p}}} \nabla T \right) + s_{\mathrm{T}},$$

(1)

where $\rho$ is the air density, $t$ is time, $\overrightarrow{v}$ is the air velocity vector, $p$ is the static pressure, $\mu$ is the molecular viscosity, $I$ is the dynamic tensor, $\rho \overrightarrow{g}$ and $\overrightarrow{F}$ are the gravitational and external body force $k_{\mathrm{T}}$ is the coefficient of heat transfer, $C_{\mathrm{p}}$ is the specific heat capacity, and $s_{\mathrm{T}}$ is the viscous dissipation energy.

The air in the roadway is a typical turbulent flow, and the most widely used standard k-epsilon turbulence model was adopted to simulate the flow behaviour [18, 19]. The turbulence kinetic energy, $k$ and its rate of dissipation, $\varepsilon$, can be obtained from the following equations [20]:

$$\frac{\partial}{\partial t}(\rho k) + \frac{\partial}{\partial x_i}(\rho k u_i) = \frac{\partial}{\partial x_j}\left[\left(\mu + \frac{\mu_\tau}{\sigma_k}\right)\frac{\partial k}{\partial x_j}\right]$$

$$+ G_k + G_b - \rho\varepsilon - Y_m + s_K,$$

$$\frac{\partial}{\partial t}(\rho\varepsilon) + \frac{\partial}{\partial x_i}(\rho\varepsilon u_i) = \frac{\partial}{\partial x_j}\left[\left(\mu + \frac{\mu_\tau}{\sigma_\varepsilon}\right)\frac{\partial\varepsilon}{\partial x_j}\right]$$

$$+ C_{1\varepsilon}\frac{\varepsilon}{k}(G_k + G_{3\varepsilon}G_b) - C_{2\varepsilon}\rho\frac{\varepsilon^2}{k} + s_\varepsilon, \tag{2}$$

where $G_k$ and $G_b$ denote the generation of turbulence kinetic energy due to the mean velocity gradients and buoyancy, respectively. $Y_m$ denotes the contribution of the fluctuating dilatation. The values of $C_{1\varepsilon}$, $C_{2\varepsilon}$, $G_{3\varepsilon}$, $S_k$, and $s_\varepsilon$ are 1.44, 1.92, 0.09, 1.0, and 0.85, respectively.

The convergence criteria were set to 10–5 for all variables, mass, momentum, $k$, and $\varepsilon$ to ensure an appropriate and reliable convergence. The energy equation was not activated since the air in the roadway is assumed to be viscous and incompressible, and there was no heat transfer.

### 2.2. The Model of Dust Behaviour.

The discrete phase model follows the Euler–Lagrange method, where the continuous phase is solved by Navier–Stokes equations, and the second phase is dispersed in the continuous phase [19]. For the dispersed second phase, the particle-particle interactions can be neglected and it is required a low volume fraction with no more than 10%. The trajectory of dust particles is computed by integrating the force balance on the particle. The particle force balance equation is as follows [17]:

$$\frac{dv_p}{d_t} = \frac{18\mu}{\rho_p d_p^2}\frac{C_D\rho d_p\left|\vec{v}_p - \vec{v}\right|}{24v}\left(\vec{v} - \vec{v}_p\right)$$

$$+ \frac{\vec{g}(\rho_p - \rho)}{\rho_p} + \vec{F}, \tag{3}$$

where $\vec{v}_p$ and $\vec{v}$ are the particle and fluid phase velocity, respectively, $\mu$ is the molecular viscosity of the air, $\rho_p$ and $\rho$ are the density of the particle and the fluid phase, $d_p$ is the particle diameter, and $\vec{F}$ is an additional acceleration term. $C_D$ denotes the drag coefficient, which is defined as [17]

$$C_D = a_1 + \frac{a_2}{R_e} + \frac{a_3}{R_e^2}, \tag{4}$$

where $R_e$ is relative Reynolds number and $a_1$, $a_2$, and $a_3$ are constants that apply over several ranges of Re.

### 2.3. Two-Way Coupling Model.

When calculating the trajectory of the particle, ANSYS Fluent will track the mass and momentum gained or lost by the particle stream, and these quantities can be incorporated in the subsequent continuous phase calculations. Thus, the continuous phase not only impacts the discrete phase but also incorporates the effect of the particle trajectories on the continuum [17]. As shown in
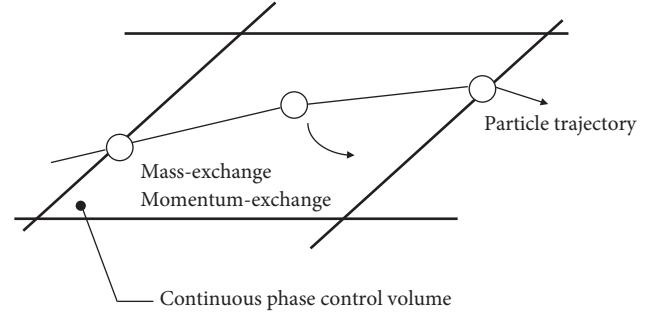


FIGURE 1: Two-way coupling model.

Figure 1, this two-way coupling is accomplished by alternately solving the discrete and continuous phase equations until the solutions in both phases have stopped changing.

### 2.3.1. Mass Exchange.

The mass exchange from the discrete phase to the continuum is calculated in ANSYS Fluent by examining the change in the mass of a particle when it passes through each control volume in the computational model. The mass change is computed as [17]

$$M = \frac{\Delta m_p}{m_p, 0}\dot{m}_p, 0. \tag{5}$$

### 2.3.2. Momentum Exchange.

The momentum exchange from the continuous phase to the discrete phase is computed in ANSYS Fluent by examining the change in momentum of a particle as it passes through each control volume in the computational model. This momentum change is computed as [17]

$$F = \sum\left(\frac{18\mu C_D\text{Re}}{\rho_p d_p^2}(v_p - v) + F_{\text{other}}\right)\dot{m}_p\Delta t, \tag{6}$$

where $\dot{m}_p$ is the mass flow rate of the particles, $\Delta t$ is the time step, and $F_{\text{other}}$ is other interaction forces.

### 2.4. Dust Diffusion Mechanism.

Dust diffusion in deep mining results from various external factors. Under the initial conditions, the dust generated by blasting and digging obtains an initial velocity through mechanical force. After moving to the roadway, the dust starts to move in the direction of the wind flow by the ventilation airflow. During this period, the dust is mainly affected by the force exerted by the resistance from the fluid, buoyancy, and its own gravity [20]. In order to facilitate the theoretical analysis, the dust diffusion can be simplified to one-dimensional longitudinal diffusion of equal strength sources. Starting from $t = 0$ s, the dust diffusion is continuously added with dust diffuser somewhere. The diffusion equation is as follows [20]:

$$\frac{\partial\rho}{\partial t} + V\frac{\partial\rho}{\partial x} = K\cdot\frac{\partial^2\rho}{\partial^2 x}, \tag{7}$$

where $K$ denotes a diffusion coefficient, $\rho$ denotes the average dust concentration, $V$ denotes the average flow velocity, and $t$ denotes diffusion time.

## 3. Numerical Modelling

*3.1. Model Geometry and Meshing.* Considering the actual situation at Woxi Pithead mining face, a simplified physical model was established (Figure 2). As shown, the three-dimension computational model consisted of three parts, including a mining roadway, a pressure air duct which injected fresh air into the working face, and an exhaust air duct which absorbed the contaminated air. The roadway was 40 m in length, 3.2 m in width, and 3.15 m high, resulting in a cross section of 9 m$^2$. The diameter of both the pressure air duct and the exhaust air duct was 0.6 m, and the distance between the central axes of the ducts and the ground was 1.8 m. The numerical model was meshed by tetrahedral unstructured grids with 647,994 elements using Ansys ICEM software.

Mesh independence test was carried out by generating three different grid sizes, a fine grid (1,238,024 elements), a medium grid (647,994 elements), and a coarse grid (235,675 elements). It was found that the fine grid had no appreciable change on the result except the higher computational cost compared to the medium grid, and as for the coarse grid, the grid quality was limited and difficult to improve, which cannot meet the model requirement. Therefore, a medium grid with 647,994 elements was acceptable and reliable to assure the mesh independence.

*3.2. Simulation Conditions.* Considering trial tests and engineering situations, the boundary conditions for airflow migration were determined as follows: the velocity parameter was used to control both the pressure air duct outlet and the exhaust air duct inlet. The boundary type of the roadway outlet was set as the outflow. No-slip wall boundary was adopted for the other surfaces. As for the dust particles, the "reflect" boundary condition was selected for the roof, floor, and sides of the roadway while the "escaped" boundary condition was set for the pressure air duct outlet, exhaust air duct inlet, and the roadway outlet. Tables 1 and 2 show the parameter settings of the continuous phase model and the discrete phase model, respectively, and Table 3 shows the parameter settings of dust.

*3.3. Simulation Scenarios.* The dust removal effect can be influenced by many factors. Considering the engineering situation, four parameters were selected in this paper to investigate their influence on the dust removal effect. The investigated parameters were the distance of pressure air duct outlet from working face ($L_{\text{p-outlet}}$), the distance of exhaust air duct inlet from working face ($L_{\text{e-inlet}}$), the ratio of pressing air volume to absorption air volume ($K$), and the installation height of the air duct ($H$). These parameters were introduced, and their simulation ranges were discussed. The simulation scenarios are shown in Table 4 based on trial tests and engineering experiences. In order to perform parameter optimization, the parameters were simulated in sequence. To be more specific, the optimal value of the $L_{\text{p-outlet}}$ can be obtained through case 1 to case 3, and then the optimal $L_{\text{p-outlet}}$ was used as the simulation setting value of the next parameter, $L_{\text{e-inlet}}$ which can be obtained through case 4 to case 7. Finally, all parameters were selected, which were considered as the optimal parameters in this paper.

*3.3.1. The Values of $L_{p\text{-}outlet}$ and $L_{e\text{-}inlet}$.* The values of $L_{\text{p-outlet}}$ and $L_{\text{e-inlet}}$ will affect the wind field thus the migration and diffusion of the dust. If the value of $L_{\text{p-outlet}}$ is larger, the airflow cannot reach the heading face. To effectively discharge the dust and gunpowder on the working face and ensure that the air duct is not destroyed during the mining blasting, the values of $L_{\text{p-outlet}}$ and $L_{\text{e-inlet}}$ were set as $(4-8)\sqrt{s}$ ($2\sqrt{s}$ gradient increments) and $(0.5-1.5)\sqrt{s}$ ($0.5\sqrt{s}$ gradient increments), respectively. $S$ denotes the area of the cross section for the roadway, which was about 9 m$^2$ in this paper.

*3.3.2. The Value of $K$.* The ratio of pressing air volume to absorption air volume has a great influence on dust diffusion. If the ratio is higher, it will cause the fallen dust to be kicked up again and increase the dust content in the air. However, with a small ratio, the fresh air is not enough to dilute and discharge the dust in time. A field test was conducted to find that the pressing air volume was 250 m$^3$/min. The different values of $K$ were obtained by changing the absorption air volume. The value of $K$ was set as 0.8~1.2 (0.2 gradient increments).

*3.3.3. The Value of $H$.* The installation height of the ventilation duct not only depends on the effectiveness of dust removal but also on the convenience of replacement and maintenance. The value of $H$ was set as 1.4~1.8 (0.2 gradient increments).

## 4. Model Validation and Verification

To validate the simulation results of airflow field and dust behaviour, a series of site tests were designed and carried out. As shown in Figure 2, the air velocities at the three plane points, including point A (0.8 m, 1.0 m), point B (2.4 m, 1.0 m), and point C (1.6 m, 1.5 m), with a variety of Z coordinates away from the heading face, including 5 m, 10 m, 15 m, 20 m, 25 m, 30 m, and 35 m, were measured and compared with the simulation results. The airflow velocities were measured by AR866A anemometer. Figure 3 shows the comparison of the simulation velocity and in situ measured velocity. It can be found that the simulation results showed a good agreement with the in situ measurement results.

## 5. Results and Discussion

*5.1. Simulation Results of Airflow Field.* The airflow field in the mining working face was simulated and analyzed. As shown in Figures 4 and 5, the fresh air emitted from the pressure air duct outlet migrated toward the excavation face
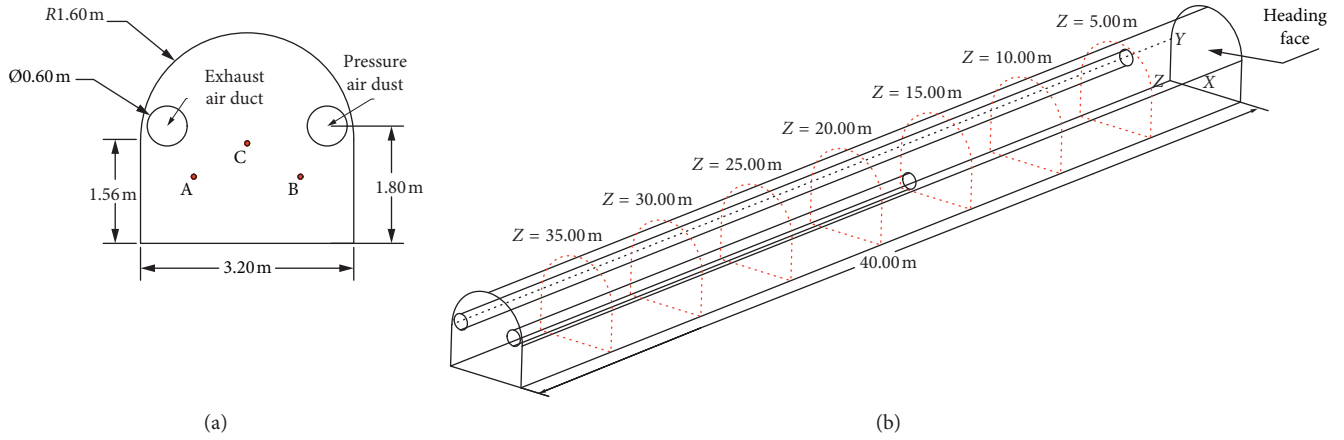
FIGURE 2: The diagram of the excavation working face. (a) The cross section of the physical model and (b) three-dimensional computational model.

TABLE 1: Parameter settling of the continuous phase model.

| Setting options | Setting states | Setting options | Setting states |
|---|---|---|---|
| Solver | Pressure based | Air density | $1.225 \text{ kg/m}^3$ |
| Time | Steady | Air viscosity | $1.79e - 05$ |
| Velocity formulation | Absolute | Velocity inlet of the exhaust air duct | $-12.5 \text{ m/s}$ |
| Viscous model | Standard k-epsilon | Velocity inlet of the pressure air duct | $15 \text{ m/s}$ |
| Hydraulic diameter | 0.6 m | Scheme | SIMPLEC |

TABLE 2: Parameter settling of the discrete phase model.

| Setting options | Setting states | Setting options | Setting states |
|---|---|---|---|
| Solver | Pressure based | Number of continuous phase iterations per DPM iteration | 20 |
| Time | Transient | Unsteady particle tracking | On |
| Velocity formulation | Absolute | Max number of steps | 200000 |
| Discrete phase model | On | Scheme | PISO |

with a higher speed, forming a typical adherent jet field. As the airflow field moved forward, the jet cross section expanded. When the jet fluid collided and rebounded at the heading face, the airflow swung around the wall and formed an impinging jet.

Part of the rotary wind flowed along the side wall of the exhaust air duct and was sucked into the exhaust inlet then discharged from the roadway. In contrast, the remaining airflows were entrained by the jet field and formed a vortex field at the outlet of pressure air duct. However, the flow field tended to be relatively stable due to the decrease of wind velocity in the tunnel space gradually away from the air ducts.

In order to further investigate the airflow field migration along the $Z$ direction, the velocity distribution was analyzed at six roadway cross sections away from the head-on face, including 5 m, 10 m, 15 m, 25 m, 30 m, and 35 m. As shown in Figure 6, the high-speed airflow was mainly formed in the region near the location of the pressure air duct and the region below the ventilation ducts at the section $Z = 5$ m. Under the influence of the negative pressure, the airflow

TABLE 3: Parameter settling of the dust.

| Setting options | Setting states | Setting options | Setting states |
|---|---|---|---|
| Type | $SiO_2$ | Velocity | 5 m/s |
| Density | $2560 \text{ kg/m}^3$ | Diameter distribution | Rosin-rammler |
| Injection type | Surface | Max diameter | $1 \times 10^{-4} \text{ m}$ |
| Spread parameter | 1.95 | Min diameter | $1 \times 10^{-6} \text{ m}$ |
| Total flow rate | 0.016 kg/s | Mean diameter | $4.8 \times 10^{-5} \text{ m}$ |

velocity was about 2.013–4.027 m/s in the region below the exhaust air duct. At the section of $Z = 10$ m, the airflow formed a velocity gradient between 2.829 m/s and 9.902 m/s near the region of the pressure air duct. The airflow distribution was similar to the airflow field at the section of $Z = 5$ m. At the section of $Z = 15$ m, the air jet field produced by the pressure air duct led to a relatively higher velocity

TABLE 4: Simulation scenarios.

| Parameter | Case | Parameter values | | | |
| --- | --- | --- | --- | --- | --- |
| | | $L_{\text{p-outlet}}^{*}$ | $L_{\text{e-inlet}}$ | $K$ | $H$ (m) |
| $L_{\text{p-outlet}}$ | 1 | $4\sqrt{s}$ | $\sqrt{s}$ | 1.2 | 1.6 |
| | 2 | $6\sqrt{s}$ | $\sqrt{s}$ | 1.2 | 1.6 |
| | 3 | $8\sqrt{s}$ | $\sqrt{s}$ | 1.2 | 1.6 |
| $L_{\text{e-inlet}}$ | 4 | $L_{\text{p-outlet}}^{*}$ | $0.5\sqrt{s}$ | 1.2 | 1.6 |
| | 5 | $L_{\text{p-outlet}}^{*}$ | $\sqrt{s}$ | 1.2 | 1.6 |
| | 6 | $L_{\text{p-outlet}}^{*}$ | $1.5\sqrt{s}$ | 1.2 | 1.6 |
| $K$ | 7 | $L_{\text{p-outlet}}^{*}$ | $L_{\text{e-inlet}}^{*}$ | 0.8 | 1.6 |
| | 8 | $L_{\text{p-outlet}}^{*}$ | $L_{\text{e-inlet}}^{*}$ | 1 | 1.6 |
| | 9 | $L_{\text{p-outlet}}^{*}$ | $L_{\text{e-inlet}}^{*}$ | 1.2 | 1.6 |
| $H$ | 10 | $L_{\text{p-outlet}}^{*}$ | $L_{\text{e-inlet}}^{*}$ | $K^{*}$ | 1.4 |
| | 11 | $L_{\text{p-outlet}}^{*}$ | $L_{\text{e-inlet}}^{*}$ | $K^{*}$ | 1.6 |
| | 12 | $L_{\text{p-outlet}}^{*}$ | $L_{\text{e-inlet}}^{*}$ | $K^{*}$ | 1.8 |

Note. $L_{\text{p-outlet}}^{*}$, $L_{\text{e-inlet}}^{*}$, and $K^{*}$ denote the optimal value of $L_{\text{p-outlet}}$, $L_{\text{e-inlet}}$, and $K$, respectively.
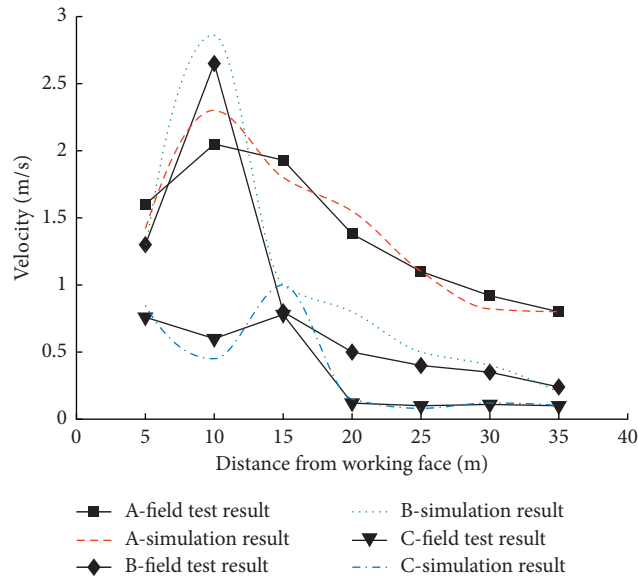


FIGURE 3: Comparison of the simulation velocity and the in situ measured velocity.

near the pressure air duct, and the maximum velocity could be up to 13.95 m/s. At the section of $Z = 25$ m, $Z = 30$ m, and $Z = 35$ m, the airflow field distribution was similar. In such cases, the velocity distribution was uniformly distributed at the cross section and the maximum velocity was observed at the bottom of the exhaust air duct. At $Z = 35$ m, the airflow was fully developed in the roadway without the influence of the airflow disturbance.

## 5.2. Sensitivity Analysis

### 5.2.1. Influence of $L_{p\text{-}outlet}$ on Dust Concentration.
Figure 7 shows the influence of $L_{\text{p-outlet}}$ (12 m, 18 m, and 24 m) on the dust concentration with $L_{\text{e-inlet}} = 3$ m, $K = 1.2$, and $H = 1.6$ m. As shown, the maximum mass concentration was $2.755 \times 10^{-3}$ kg/m$^3$ when the $L_{\text{p-outlet}}$ was 12 m, which

was extremely higher than the safety regulation values. Moreover, the dust diffusion range was the farthest with a 12 m $L_{\text{p-outlet}}$. That is caused by the short distance between the pressure air duct and the working face, resulting in a too quick dust flow under the combined action of the high jet field and the negative pressure of the exhaust duct. In such case, the dust cannot form an effective backflow, and the dirt from the ground can be pulled up again. When $L_{\text{p-outlet}}$ was increased to 18 m and 24 m, the dust mass concentration was reduced more than an order of magnitude. However, the dust diffusion range with a $L_{\text{p-outlet}}$ of 24 m was relatively high, which is caused by the long distance between the pressure air duct and the working face. Under this condition, the fresh air ejected from the pressure air duct cannot reach the excavation face, which leads to the formation of the vortex behind the jet inflexion point. The dust cannot be removed effectively due to the vortex. The dust concentration and
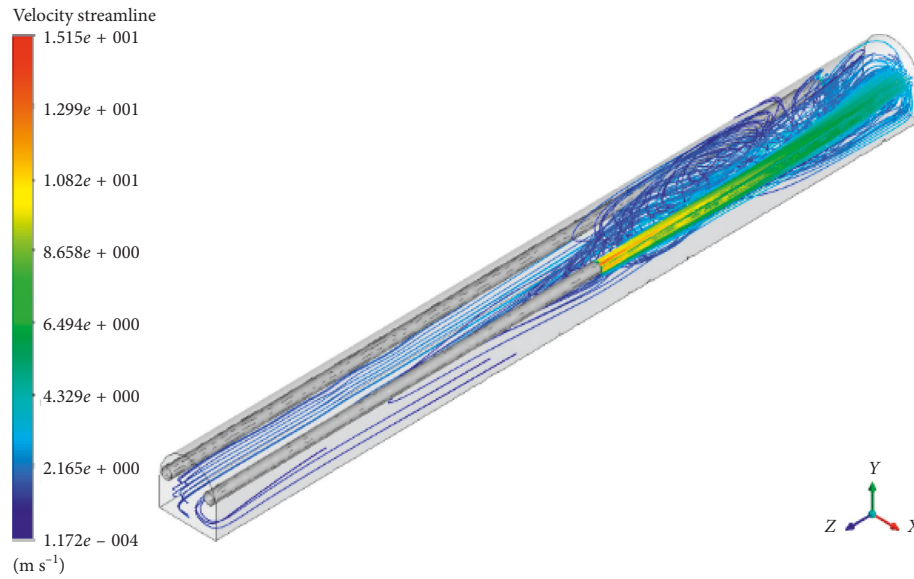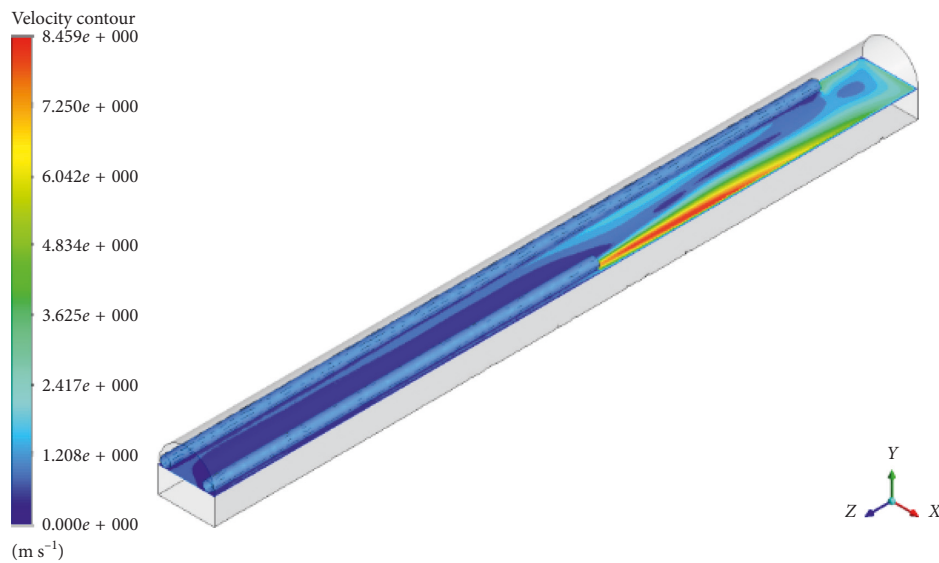
Figure 4: 3D diagram of airflow streamlines.



Figure 5: Contour of velocity at $Y = 1.5$ m.

diffusion range with a $L_{p\text{-outlet}}$ of 18 m were the lowest. That is because the value of $L_{p\text{-outlet}}$ is exactly within the effective range of the jet flow. The high-concentration dust can be diluted and removed effectively by the fully developed airflow field. Therefore, the optimal parameter of $L_{e\text{-inlet}}$ was determined to be 18 m.

### 5.2.2. Influence of $L_{e\text{-inlet}}$ on Dust Concentration.
Figure 8 shows the influence of $L_{e\text{-inlet}}$ (1.5 m, 3.0 m, and 4.5 m) on the dust concentration with $L_{p\text{-outlet}} = 18$ m, $K = 1.2$, and $H = 1.6$ m. It can be found that the maximum dust concentration was $1.61 \times 10^{-3}$ kg/m$^3$ when $L_{e\text{-inlet}}$ was 1.5 m. That is because the exhaust air duct is so close to the

mining face that the turbulent flow is formed around the working face. The dust moves with the turbulent flow and spreads out in the roadway. However, when $L_{e\text{-inlet}}$ was 3 m, the dust concentration reduced to $7.862 \times 10^{-4}$ kg/m$^3$, and the region of particle pollution was confined to the former area of the exhaust air duct. Therefore, the optimal parameter of $L_{e\text{-inlet}}$ was 3 m.

### 5.2.3. Influence of K on Dust Concentration.
The influence of $K$ (0.8, 1.0, 1.2) on the concentration of dust is shown in Figure 9 when $L_{p\text{-outlet}}$ was 18 m, $L_{e\text{-inlet}}$ was 3 m, and H was 1.6 m. As shown, the dust in the front part of the roadway was sucked into the exhaust air duct but most of the dust was
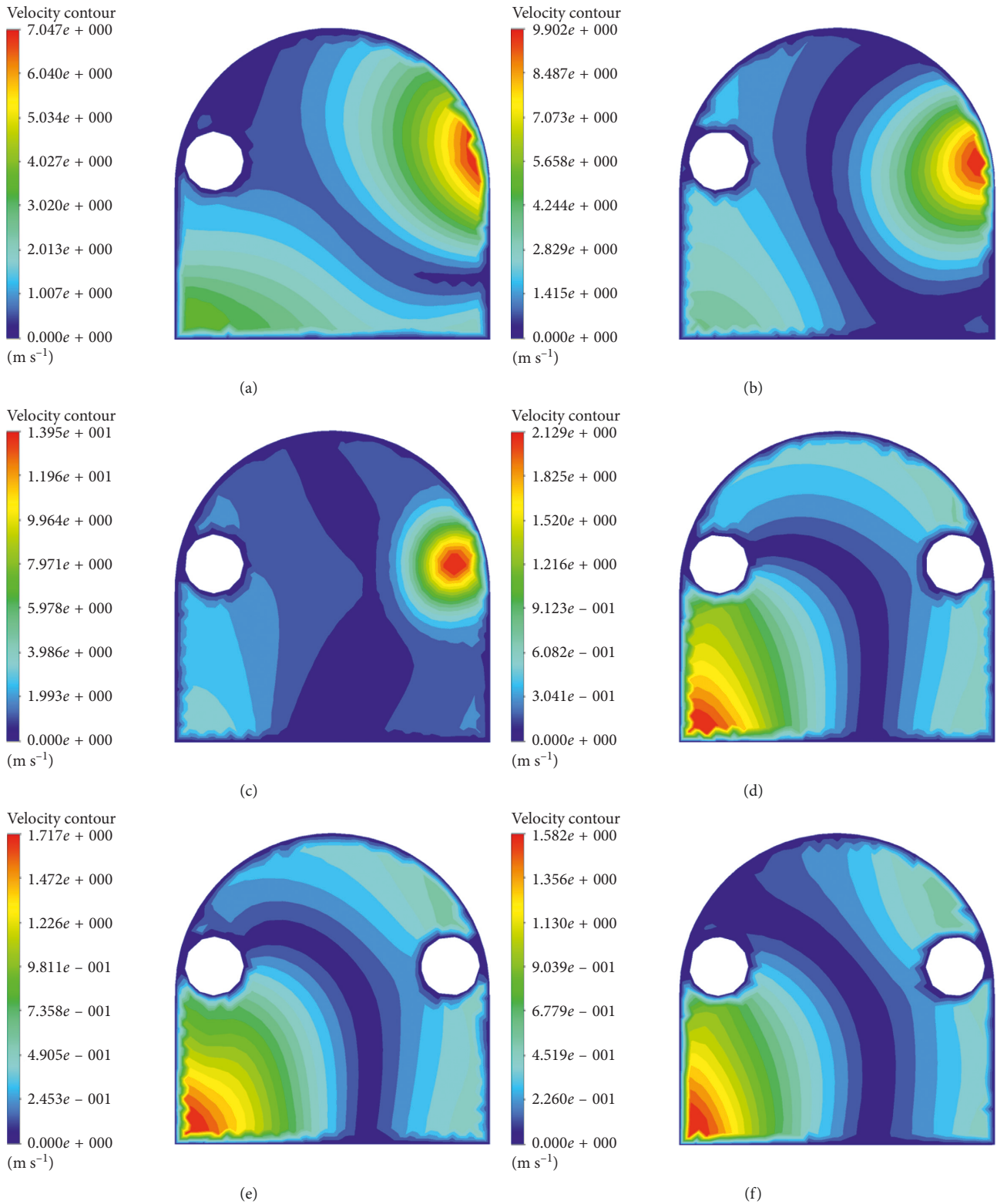
Figure 6: Contour of velocity at different regions. (a) 5 m, (b) 10 m, (c) 15 m, (d) 25 m, (e) 30 m, and (f) 35 m.

not diluted and removed when $K$ was 0.8. When the pressing air volume equalled to the absorption air volume, the dust concentration was high, and a large amount of dust

remained in the roadway. This is because the fresh air emitted from the pressure air duct migrates toward the working face. During the migration, only part of the airflow
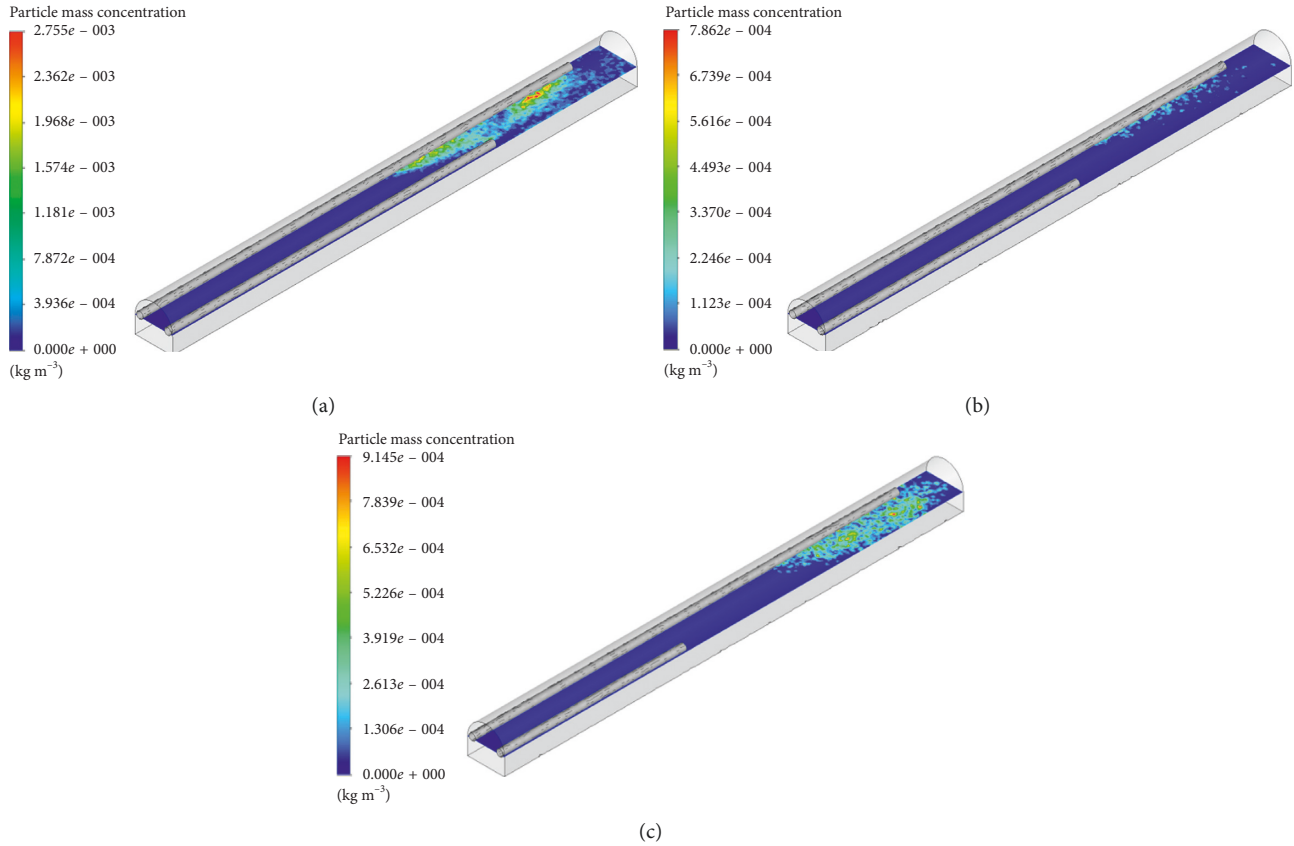
(a)



(b)



(c)

FIGURE 7: Influence of $L_{p\text{-outlet}}$ on the mass concentration of dust. (a) 12 m, (b) 18 m, and (c) 24 m.

is sucked away by the exhaust air duct, while the other part continues to move towards the roadway outlet and reduces the dust removal effect. The dust concentration and diffusion range with $K = 1.2$ were the lowest. Therefore, the optimal parameter of $K$ was 1.2.

*5.2.4. Influence of H on Dust Concentration.* Figure 10 shows the influence of $H$ (1.4 m, 1.6 m, 1.8 m) on the dust concentration with $L_{p\text{-outlet}} = 18$ m, $L_{e\text{-inlet}} = 3$ m, and $K = 1.2$. It can be seen that when $H$ was 1.4 m and 1.8 m, the dust concentration and diffusion range was high, and most of the dust remained in the roadway. However, the maximum dust concentration was reduced to $7.862 \times 10^{-4}$ kg/m$^3$ when $H$ was 1.6 m, indicating most of the dust was diluted and removed effectively. Therefore, the optimal parameter of $H$ was 1.6 m.

To fully investigate the effect of different parameter arrangement on dust removal efficiency, the dust concentration in the middle line of the roadway at the breathing zone ($y = 1.55$ m) is presented in Figure 11. As is shown in Figure 11, with the increase of distance from the working face, the overall dust concentration maintained a declining trend. Figure 11(a) shows when $L_{p\text{-outlet}}$ was 12 m, the dust concentration was the highest and can be up to $2.755 \times 10^{-3}$ kg/m$^3$, and the dust mass concentration decreased sharply when the distance from the working face was between 5 m and 13 m. When $L_{p\text{-outlet}}$ was 18 m and 24 m,

the dust concentration kept a steady downward trend, and it can be seen that when $L_{p\text{-outlet}}$ was 18 m, the dust concentration was the lowest. Figure 11(b) shows when $L_{e\text{-inlet}}$ was 4.5 m, the dust concentration was the highest, and when $L_{e\text{-inlet}}$ was 3 m, the dust concentration was $8.25 \times 10^{-4}$ kg/m$^3$, which is the lowest. As is shown in Figure 11(c) and Figure 11(d), it can be seen that the lowest dust concentration was achieved when $K$ was 1.2 and $H$ was 1.6 m.

## 6. Conclusions

Based on the theory of gas-solid two-phase flow, an airflow-dust coupled model was constructed to assess the airflow migration and dust behaviour in the hybrid ventilation system. The far-pressing-near-absorption (FPNA) hybrid ventilation system was established to simulate the distribution of airflow field. The results show that there were four regions for the airflow field, namely, the jet zone, the recirculation zone, the vortex zone, and the mixing zone of pressure and exhaust airflow. Among them, the reasonable mixing zone of pressure and exhaust airflow could form the air barrier to prevent dust escape, which played an important role in improving the efficiency of dust removal effect.

Through the comprehensive sensitivity study, all four parameters, including $L_{p\text{-outlet}}$, $L_{e\text{-inlet}}$, $K$, and $H$, were found to have an important influence on the mass concentration of dust. The optimal ventilation layout parameter was obtained.
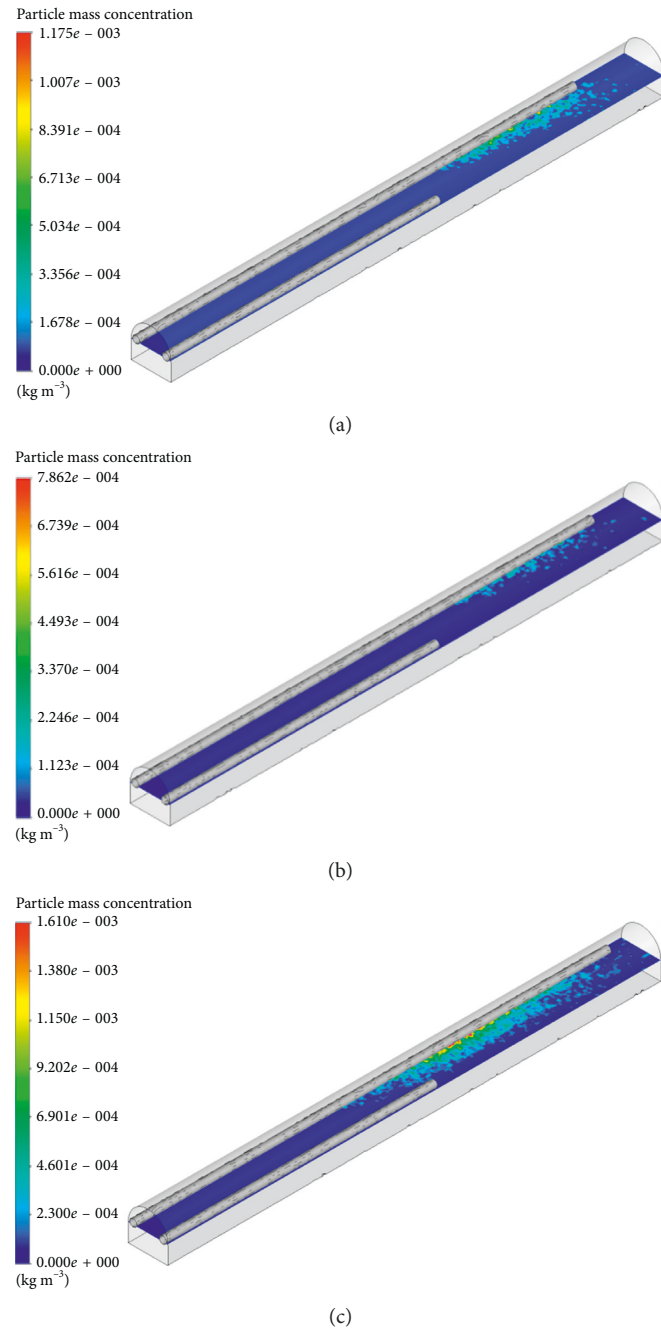
Particle mass concentration

1.175*e* − 003

1.007*e* − 003

8.391*e* − 004

6.713*e* − 004

5.034*e* − 004

3.356*e* − 004

1.678*e* − 004

0.000*e* + 000
(kg m$^{-3}$)

(a)

Particle mass concentration

7.862*e* − 004

6.739*e* − 004

5.616*e* − 004

4.493*e* − 004

3.370*e* − 004

2.246*e* − 004

1.123*e* − 004

0.000*e* + 000
(kg m$^{-3}$)

(b)

Particle mass concentration

1.610*e* − 003

1.380*e* − 003

1.150*e* − 003

9.202*e* − 004

6.901*e* − 004

4.601*e* − 004

2.300*e* − 004

0.000*e* + 000
(kg m$^{-3}$)

(c)

FIGURE 8: Influence of $L_{e\text{-inlet}}$ on the mass concentration of dust. (a) 1.5 m, (b) 3.0 m, and (c) 4.5 m.

(a)



(b)



(c)
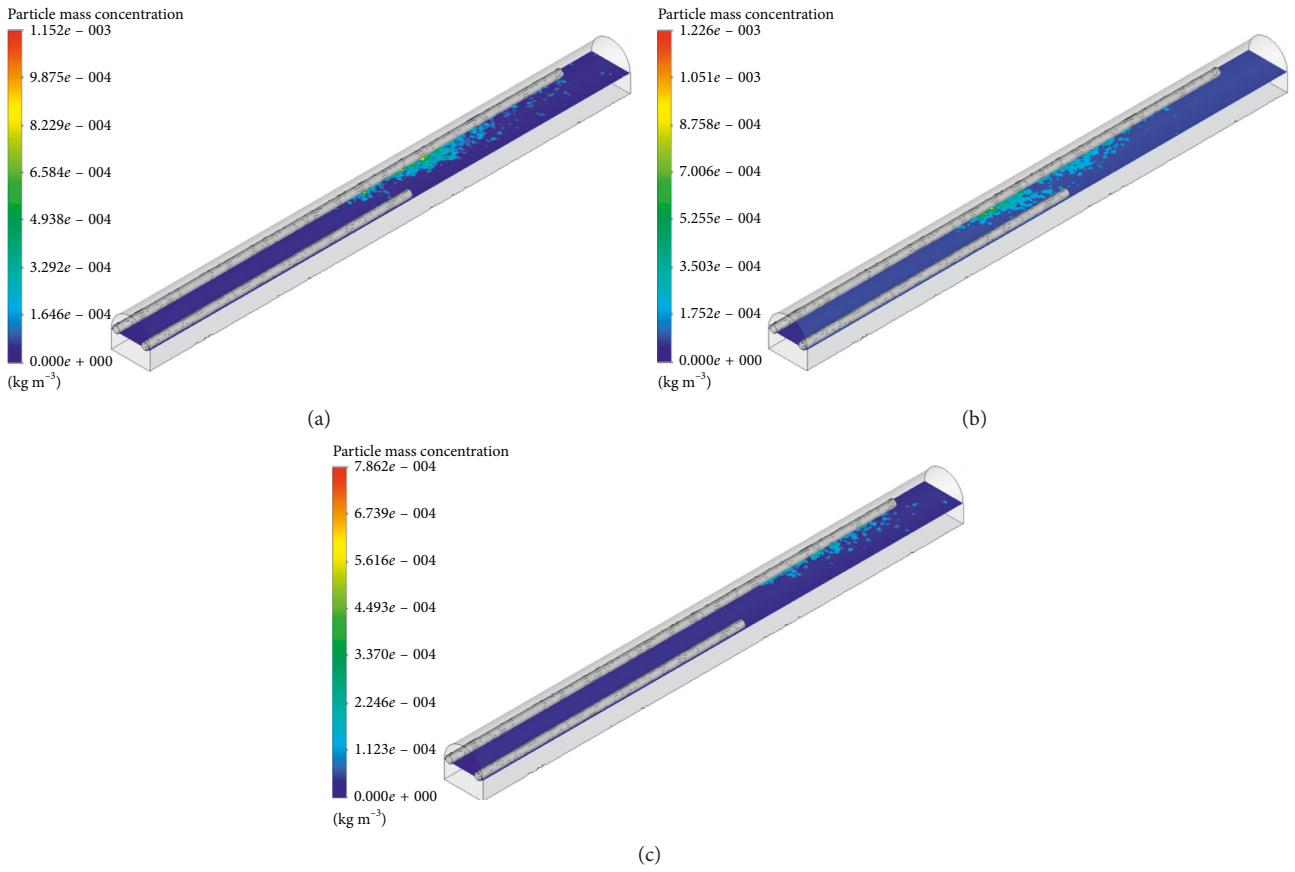
FIGURE 9: Influence of K on the mass concentration of dust. (a) 0.8 m, (b) 1.0 m, and (c) 1.2 m.
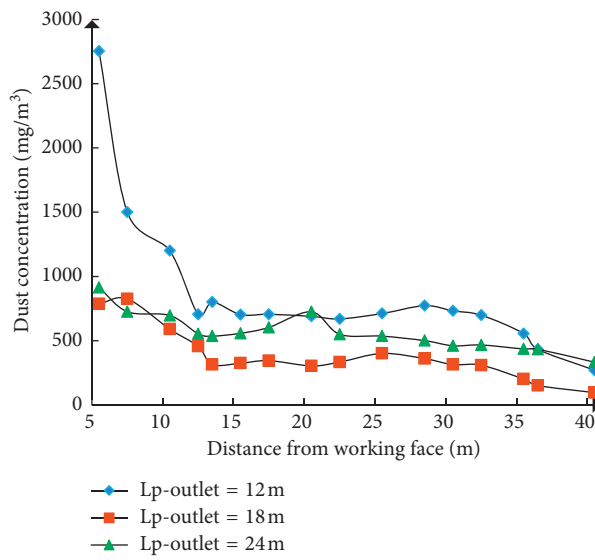


(a)



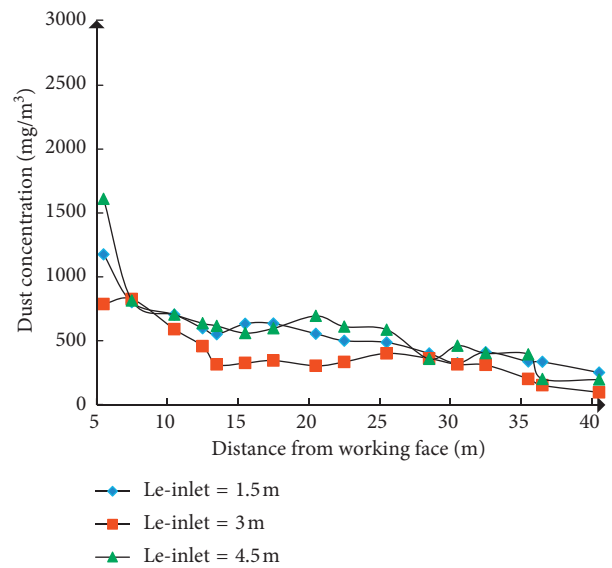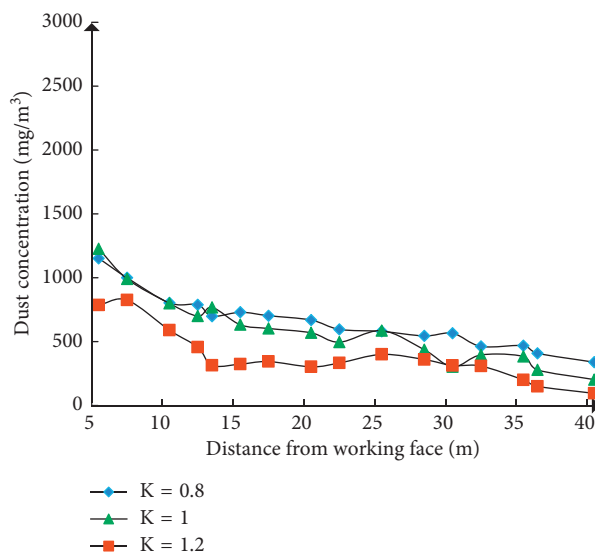(b)
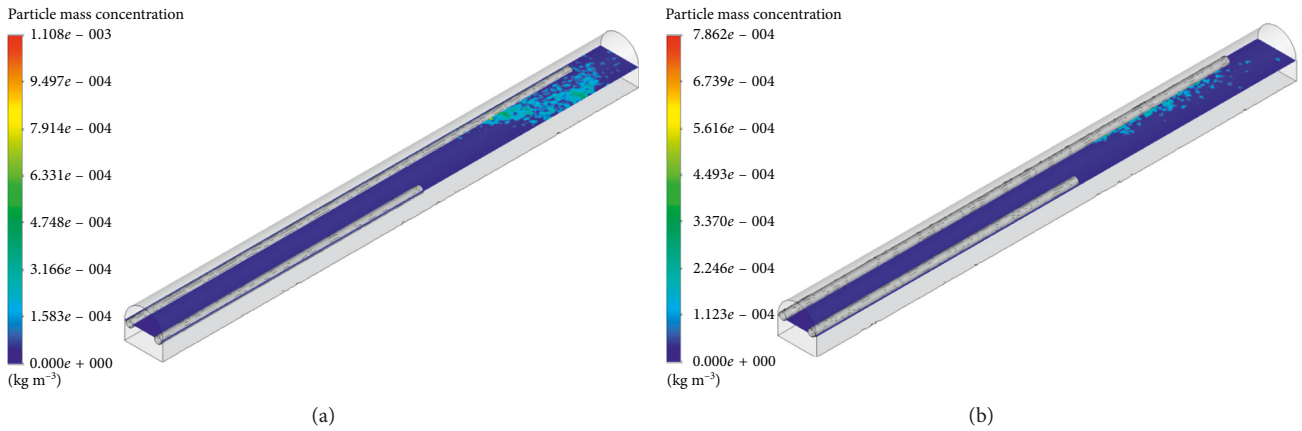
FIGURE 10: Continued.
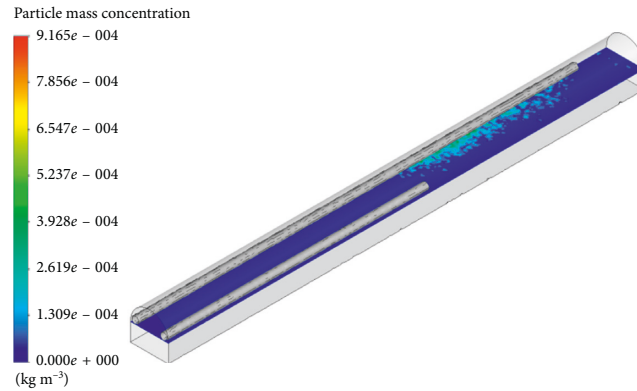
(c)

FIGURE 10: Influence of H on the mass concentration of dust. (a) 1.4 m, (b) 1.6 m, and (c) 1.8 m.



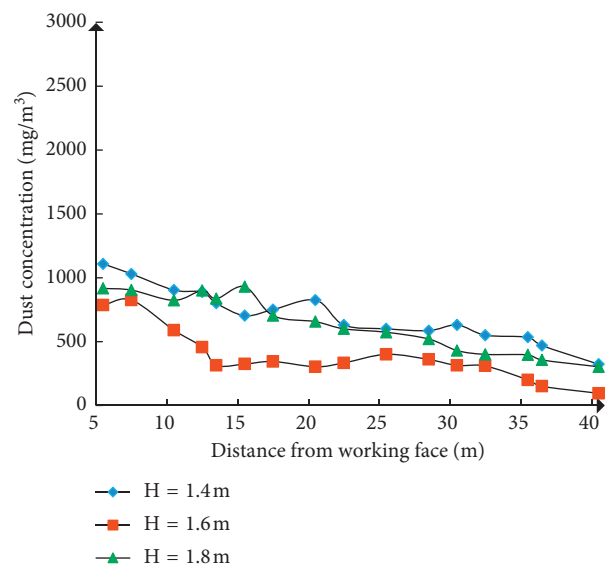(a)



(b)



(c)



(d)

FIGURE 11: Dust concentration along the roadway at the breathing zone under the influence of different parameters. (a) $L_{p\text{-outlet}}$, (b) $L_{e\text{-inlet}}$, (c) $K$, and (d) $H$.

It is concluded that when $L_{\text{p-outlet}}$ was 18 m, $L_{\text{e-inlet}}$ was 3 m, $K$ was 1.2, and $H$ was 1.6 m, the dust concentration was reduced to the safety standard, and the dust removal effect was the best.

## Data Availability

The data used to support the findings of this study are included within the article.
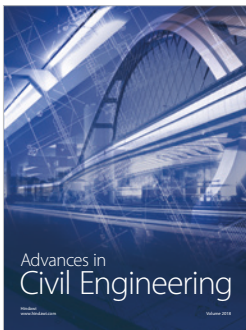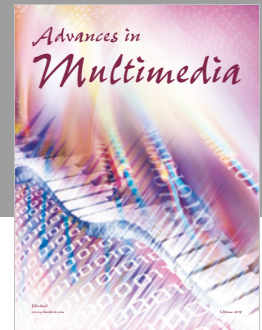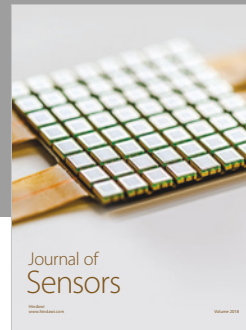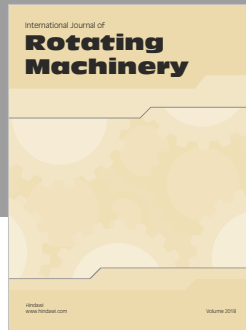
## Conflicts of Interest

The authors declare that there are no conflicts of interest regarding the publication of this paper.

## Acknowledgments

## References

[1] H. Wang, D. Wang, W. Ren, X. Lu, F. Han, and Y. Zhang, "Application of foam to suppress rock dust in a large cross-section rock roadway driven with road header," *Advanced Powder Technology*, vol. 24, no. 1, pp. 257–262, 2013.

[2] F. N. Kissell, "Handbook for dust control in mining," *Niosh Information Circular*, vol. 54, no. 9, pp. 969–976, 2003.

[3] D. K. Lee, "A computational flow analysis for choosing the diameter and position of an air duct in a working face," *Journal of Mining Science*, vol. 47, no. 5, pp. 664–674, 2011.

[4] D. Wang, *Mine Dusts*, Science Press, Beijing, China, 2015.

[5] T. Zhao, *Technology of Dust Control in Underground Mines*, China Coal Industry Publishing House, Beijing, China, 2007.

[6] P. Wang, T. Feng, and R. Liu, "Numerical simulation of dust distribution at a fully mechanized face under the isolation effect of an air curtain," *International Journal of Mining Science and Technology*, vol. 21, no. 1, pp. 65–69, 2011.

[7] W. Cheng, H. Yu, G. Zhou, and W. Nie, "The diffusion and pollution mechanisms of airborne dusts in fully-mechanized excavation face at mesoscopic scale based on CFD-DEM," *Process Safety and Environmental Protection*, vol. 104, pp. 240–253, 2016.

[8] C. Özgen Karacan, "Development and application of reservoir models and artificial neural networks for optimizing ventilation air requirements in development mining of coal seams," *International Journal of Coal Geology*, vol. 72, no. 3-4, pp. 221–239, 2007.

[9] G. Zhou, Q. Zhang, R. Bai, T. Fan, and G. Wang, "The diffusion behavior law of respirable dust at fully mechanized caving face in coal mine: CFD numerical simulation and engineering application," *Process Safety & Environmental Protection*, vol. 106, pp. 117–128, 2017.

[10] F. E. Camelli, G. Byrne, and R. Löhner, "Modeling subway air flow using CFD," *Tunnelling and Underground Space Technology*, vol. 43, no. 7, pp. 20–31, 2014.

[11] Q. Wang, D. Wang, H. Wang, F. Han, X. Zhu, and Y. Tang, "Optimization and implementation of a foam system to suppress dust in coal mine excavation face," *Process Safety and Environmental Protection*, vol. 96, pp. 184–190, 2015.

[12] J. Toraño, S. Torno, M. Menéndez, and M. Gent, "Auxiliary ventilation in mining roadways driven with roadheaders: validated CFD modelling of dust behavior," *Tunnelling and Underground Space Technology incorporating Trenchless Technology Research*, vol. 26, no. 1, pp. 201–210, 2011.

[13] K. J. Candra, S. A. Pulung, and M. A. Sadashiv, "Dust dispersion and management in underground mining faces," *International Journal of Mining Science and Technology*, vol. 24, no. 1, pp. 39–44, 2014.

[14] H. Yu, W. Cheng, L. Wu, H. Wang, and Y. Xie, "Mechanisms of dust diffuse pollution under forced-exhaust ventilation in fully-mechanized excavation faces by CFD-DEM," *Powder Technology*, vol. 317, pp. 31–47, 2017.

[15] H. R. Nazif and H. B. Tabrizi, "Development of boundary transfer method in simulation of gas–solid turbulent flow of a riser," *Applied Mathematical Modelling*, vol. 37, no. 4, pp. 2445–2459, 2013.

[16] I. Goldasteh, G. Ahmadi, and A. R. Ferro, "Monte carlo simulation of micron size spherical particle removal and resuspension from substrate under fluid flows," *Journal of Aerosol Science*, vol. 66, no. 4, pp. 62–71, 2013.

[17] ANSYS, *FLUENT Theory Guide*, ANSYS Inc., Canonsburg, PA, USA, 2014.

[18] J. Serafin, A. Bebcak, A. Bernatik, P. Lepik, M. Mynarz, and M. Pitt, "The influence of air flow on maximum explosion characteristics of dust–air mixtures," *Journal of Loss Prevention in the Process Industries*, vol. 26, no. 1, pp. 209–214, 2013.

[19] S. A. Silvester, I. S. Lowndes, and D. M. Hargreaves, "A computational study of particulate emissions from an open pit quarry under neutral atmospheric conditions," *Atmospheric Environment*, vol. 43, no. 40, pp. 6415–6424, 2009.

[20] D. C. Wilcox, *Turbulence Modeling for CFD*, DCW Industries Inc., La Cañada Flintridge, CA, USA, 1993.

The Scientific World Journal

International Journal of
Rotating Machinery

Journal of
Sensors

Advances in
Multimedia

Journal of
Engineering

Advances in
Civil Engineering

Journal of
Control Science
and Engineering

Journal of
Robotics

Hindawi

Submit your manuscripts at
www.hindawi.com

Journal of
Electrical and Computer
Engineering

Advances in
OptoElectronics

VLSI Design

International Journal of
Navigation and
Observation

Modelling &
Simulation
in Engineering

International Journal of
Aerospace
Engineering

International Journal of
Chemical Engineering

International Journal of
Antennas and
Propagation

Active and Passive
Electronic Components

Shock and Vibration

Advances in
Acoustics and Vibration